Optically selective SiC-based nanocomposite objects derived from titanium and boron-modified polycarbosilanes

Maxime Balestrat, Maxime Cheype, Pierre Carles, Xavier Deschanels, Audrey Soum-Glaude, Christel Gervais, Fabrice Rossignol, Nicolas Pradeilles, Samuel Bernard

Open Ceramics 14 (2023) 100353

Contents lists available at ScienceDirect

Open Ceramics

journal homepage: www.sciencedirect.com/journal/open-ceramics

Optically selective SiC-based nanocomposite objects derived from titanium and boron-modified polycarbosilanes

Maxime Balestrat [a,**], Maxime Cheype [a], Pierre Carles [a], Xavier Deschanels [b], Audrey Soum-Glaude [d], Christel Gervais [c], Fabrice Rossignol [a], Nicolas Pradeilles [a], Samuel Bernard [a,*]

[a] Univ. Limoges, CNRS, IRCER, UMR 7315, F-87000 Limoges, France
[b] ICSM, CEA, CNRS, Univ. Montpellier, ENSCM, Marcoule, Bagnols-sur-Cèze, France
[c] Sorbonne Université, CNRS, Collège de France, Laboratoire Chimie de la Matière Condensée de Paris, 4 Place de Jussieu, 75005, Paris, France
[d] Laboratoire PROMES-CNRS, 7 rue du Four Solaire, 66120, Font-Romeu Odeillo, France

ARTICLE INFO

Handling Editor: Dr P Colombo

Keywords:
SiC
TiC
Nanocomposites

ABSTRACT

Herein, we introduce a bottom-up material design approach of optically selective SiC-based nanocomposite objects. Precursors have been firstly synthesized by reaction of allylhydridopolycarbosilane with titanium and boron complexes before a pyrolysis at 1000 °C in flowing argon to deliver single-phase amorphous Si–Ti–C–N(B, H) ceramics. The later was then heat-treated up to 1800 °C under argon. Relatively dense nanocomposites made of TiC_xN_{1-x} ($0 \leq x \leq 1$) nanocrystals homogeneously formed *in situ* in a SiC_xN_{4-x}-type phases ($0 \leq x \leq 4$) have been isolated after heat-treatment at 1400 °C. Above 1400 °C, our experimental data showed a continuous evolution of carbon and nitrogen contents up to 1800 °C due to carbothermal reduction reactions forming carbide phases while releasing nitrogen-containing species. Thus, heat-treatment at 1800 °C led to porous and fully crystallized TiC(N)/SiC(B) nanocomposites that displayed a maximal optical selectivity of 1.67 measured at room temperature; a value significantly increased compared to the SiC(B) counterpart.

1. Introduction

Producing sustainable, renewable and low CO_2 emission electricity is a worldwide challenge. In an increasingly carbon-constrained world, solar energy technologies represent one of the least carbon-intensive means of electricity generation. Among such technologies, Concentrating Solar Power (CSP) plants are utility-scale generators that produce electricity by using mirrors or lenses to reflect and efficiently concentrate (focus) the sun's light energy onto selective solar absorbers (SSAs). The latter - surfacic (*e.g.*, tubes) or volumetric (*e.g.*, honeycomb structures) - are designed to maximize sunlight absorption and minimize the heat loss that would naturally be generated from the surface as infrared radiation [1,2].

The operational temperatures range of the SSAs is categorized as low (< 100 °C), mid (100 °C < T < 400 °C) and high (T > 400 °C) temperature [3]. Currently, SSA work at a maximum temperature of 700 °C [4]. However, photothermal conversion of solar radiation will constitute a source of energy of significant importance for a large number of applications if higher temperatures – typically above 900 °C - are reached. This will allow improving the efficiency of the thermal-to-electricity conversion with the consequence of increasing the Carnot efficiency of the power generation system [3,5].

Silicon carbide (SiC) offers unique features such as a light weight, an excellent thermal shock resistance performance, a high strength, an oxidation resistance, and a grey-black color for high temperature applications compatible with the operating conditions of further CSP systems [6,7]. Its oxidation resistance is linked to the formation of a passivating oxide layer which provides a thermal stability up to ~1400 °C [8]. However, despite good sunlight absorption in the solar spectrum, SiC has a high thermal emittance, leading to a poor optical selectivity [9].

Group IV borides, carbides or even nitrides are propitious as solar absorbers according to their inherent spectral selectivity and lower thermal emittance [9–15]. TiC is one of the prominent choices [15,16].

* Corresponding author.
** Corresponding author.
E-mail addresses: maxime.balestrat@unilim.fr (M. Balestrat), samuel.bernard@unilim.fr (S. Bernard).

https://doi.org/10.1016/j.oceram.2023.100353
Received 14 September 2022; Received in revised form 2 February 2023; Accepted 26 March 2023
Available online 28 March 2023

TiN also exhibits an inherent spectral selectivity which can be used for designing SSAs [17]. However, transition metal carbides and nitrides tend to oxidize in the targeted operating temperature range [18–20]. Therefore, to maximize the energy absorbed by the SSAs while the heat loss from them to the environment is minimized and their stability preserved above 900 °C, engineered composites combining a robust and durable matrix such as SiC and optical selective materials among group IV borides, carbides or nitrides represent the future of SSAs.

Excellent spectral selectivity has been recently attributed to nanocomposite structures made of MN precipitates (M = Cr) distributed in an AlN(O) matrix [21]. It has been particularly shown that the incident light was scattered by the CrN nanocrystallites and the optical path was enlarged. With the particle density increasing, coupling of plasmons between neighboring particles even took place, beneficial to the transmission of heat [22]. However, such nanocomposites are exclusively prepared as coatings (=surfacic) and cannot offer a large flexibility in terms of available compositions. Furthermore, the AlN(O) matrix tends to oxidize in the targeted operating temperatures.

Recent reports suggested that the Polymer-Derived Ceramics (PDCs) route is a convenient way to synthesize nanoscaled transition metal nitrides (TMNs) and/or carbides (TMCs) into a robust and covalently-bonded silicon nitride (Si_3N_4) and/or carbide (SiC) matrix [23–33]. Furthermore, this route can be associated to a shaping process such as warm-pressing (WP) or a sintering step [34,35] to form both volumetric and surfacic SSAs.

Following this strategy, the synthesis and processing of SiC-based nanocomposites upon modification of allylhydridopolycarbosilane (AHPCS) with tetrakis(dimethylamino)titanium ($Ti[N(CH_3)_2]_4$) and/or borane dimethylsulfide ($BH_3{\cdot}S(CH_3)_2$, BDMS) is addressed. The schematic representation of our approach is described in Fig. 1. The material has been characterized at each step of the process and we propose extensive structural and textural characterizations of the final nanocomposites. As a proof of concept, we explored the hemispherical reflectance of these materials at room temperature (RT) and demonstrated their promising optical selectivity.

2. Experimental methods

2.1. Materials

The synthesis of the precursor is carried out in a purified argon atmosphere passing through a column of phosphorus pentoxide and then through a vacuum/argon line by means of standard Schlenk techniques. The cleaned glassware is stored in an oven at 95 °C overnight before being connected to the vacuum/argon line, assembled and pumped under vacuum for 30 min and then filled with argon. All chemical products are handled in an argon-filled glove box (Jacomex, Campus-type; O_2 and H_2O concentrations kept at ≤0.1 ppm and ≤0.8 ppm, respectively). Toluene (99.85%, Extra Dry over Molecular Sieve, Acro-Seal(R)) was purchased from Acros Organics™. Allylhydridopolycarbosilane (AHPCS labeled SMP-10, Starfire Systems® Incorporation, New York, USA), with a density of 0.998 g cm^{-3} was stored in a freezer and used as-received. Anal. Found (wt%): Si 54.8, C 35.0, H 8.3, O 1.9. $[Si_{1.0}C_{1.5}H_{4.2}]_n$ (*Normalyzed to total 100 wt % (total of wt% was 98.5 wt%) and reference to* $Si_{1.0}$. *Oxygen content (below 2 wt%) omitted in the empirical formulae*). FTIR (ATR/cm^{-1}): ν (C–H) = 3076 (s), 3010 (s), 2954 (w), 2910 (s), 2895 (m), 2852 (m); ν (Si–H) = 2121 (vs); δ (allyl) = 1611 (m); δ (CH_2) = 1360 (m); δ (Si–CH_3) = 1251 (m); δ (Si–CH_2–Si) = 1049 cm^{-1} (s); δ (Si–H) = 940 cm^{-1} (s); δ (CH_3) = 850 cm^{-1}(s); ν (Si–C) = 780 (s). ^{1}H NMR (300 MHz, $CDCl_3$, δ/ppm): 0.05 (br, SiCH_3), 0.4 (w, SiCH_2), 1.56–1.9 (w, Si–CH_2–CH=CH_2), 3.4–3.8 (SiH_3C), 3.8–4.1 (SiH_2CH_2), 4.85–5.05 (Si–CH_2–CH=CH_2), 5.71–5.93 (Si–CH_2–CH=CH_2). Tetrakis(dimethylamino)titanium ($Ti[N(CH_3)_2]_4$, 99.99%) was obtained from Acros Organics™, stored in a fridge and used without further purification. It is labeled TDMATi. Borane dimethylsulfide $BH_3{\cdot}S(CH_3)_2$ solution (2.0 M in toluene) was obtained from Acros Organics. It is labeled BDMS.

2.2. Precursor synthesis

4.0 g of AHPCS (83.1 mmol referred to the number of monomer units in the polymer (i.e., $(Si(CH_2CHCH_2)HCH_2)_{0.1}(SiH_2CH_2)_{0.9}$) was dissolved in extra dry toluene (100 ml) in a three-necked round-bottomed flask equipped with a Teflon-coated magnetic stir bar and a magnetic stirrer. Then 3.7 g of TDMATi (16.6 mmol) was added to the solution with a syringe under argon atmosphere at room temperature to reach a molar ratio (n(Si):n(Ti)) of 5. Reaction synthesis occurred under vigorous stirring at toluene reflux for three days. On the third day, the solvent was removed under vacuum *via* an ether bridge (100 °C/ $1.5\bullet10^{-1}$ mbar) to release a viscous sample labeled **ATi**. Anal. Found (wt %): Si 27.5, Ti 10.7, C 37.8, N 13.7, H 8.7, O 1.6. $[Si_{1.0}Ti_{0.2}C_{3.2}N_{1.0}H_{8.8}]_n$ (*Normalyzed to total 100 wt % (total of wt% was 99.1 wt%) and reference to*

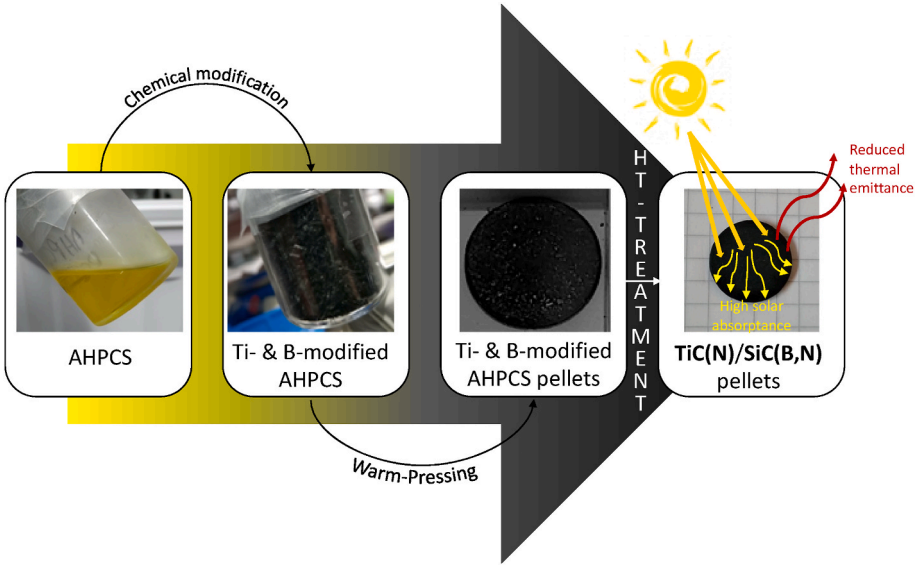

Fig. 1. Schematic diagram of the general process of designing SiC-based nanocomposite objects from Ti and B-modified polycarbosilanes and provided chemical, structural and optical fingerprints.

$Si_{1.0}$. Oxygen content (below 2 wt%) omitted in the empirical formulae). FTIR (KBr/cm^{-1}): ν (C–H) = 2960 (s), 2910 (s), 2848 (s), 2791 (s); ν(Si–H) = 2115 (s); δ (CH_3) = 1457 (s); δ (CH_2) = 1360 (m); δ(C–N) = 1294 (s); δ(Si–CH_3) = 1250 (m); δ (C–H): 1150 (s); δ (Si–CH_2–Si) = 1049 cm^{-1} (s); δ (CH_3) = 850 cm^{-1}(s); ν (Si–C) = 780 (s).

In order to form a polymer more adapted to the warm-pressing (WP) process, AHPCS was also reacted with BDMS according to our previous reports [36,37] prior to the addition of TDMATi. Thus, in a first step, the reaction of AHPCS with BDMS occurred in toluene at 0 °C according to an atomic ratio (Si:B) of 30 in a three-necked round-bottomed flask equipped with a dropping funnel and a gas inlet tube. 4.0 g of AHPCS (83.1 mmol) were introduced under argon flow in the three-necked round-bottomed flask equipped with a Teflon-coated magnetic stir bar and a magnetic stirrer, then dissolved in extra dry toluene (50 mL). In parallel, further 50 mL of toluene was introduced in the dropping funnel before adding BDMS (1.4 mL, 2.8 mmol). After cooling of the AHPCS-containing flask to 0 °C, BDMS was added dropwise to the AHPCS solution under stirring. After the addition was completed, the temperature was increased naturally up to room temperature (RT) and the mixture was stirred for three days. Then, two processes were conducted according to the targeted polymer:

(1) Solvent was removed under vacuum *via* an ether bridge (100 °C/ 1.5•10^{-1} mbar)) to release a solid sample labeled AB. This polymer served as a reference sample. Anal. Found (wt %): Si 52.9, B 0.7, C 35.6, H 8.9, O 1.9. $[Si_{1.0}B_{0.03}C_{1.6}H_{4.7}]_n$ (*Normalyzed to total 100 wt % (total of wt% was 99.3 wt%) and reference to $Si_{1.0}$. Oxygen content (below 2 wt%) omitted in the empirical formulae*). FTIR (KBr/cm^{-1}): ν (C–H) = 2910 (s), 2850 (s); ν(Si–H) = 2113 (s); δ(CH_3) = 1457 (s); δ (CH_2) = 1360 (m); δ(Si–CH_3) = 1250 (m); δ (Si–CH_2–Si) = 1049 cm^{-1} (s); δ (Si–H) = 940 cm^{-1} (s); δ (CH_3) = 850 cm^{-1}(s); ν (Si–C) = 780 (s).
(2) Solvent was kept and 3.7 g of TDMATi (16.6 mmol) was added with a syringe under argon atmosphere at RT and then reacted according to the route previously described for the synthesis of **ATi.** A solid boron- and titanium-modified AHPCS labeled **ABTi** was delivered. Anal. Found (wt %): Si 31.8, B 0.4, Ti 9.1, C 38.1, N 10.2, H 8.9, O 1.5. $[Si_{1.0}B_{0.03}Ti_{0.2}C_{2.8}N_{0.7}H_{7.8}]_n$ (*Normalyzed to total 100 wt % (total of wt% was 99.0 wt%) and reference to $Si_{1.0}$. Oxygen content (below 2 wt%) omitted in the empirical formulae*). FTIR (KBr/cm^{-1}): ν (C–H) = 2960 (s), 2910 (s), 2848 (s), 2789 (s); ν(Si–H) = 2110 (s); δ (CH_3) = 1457 (s); δ (CH_2) = 1360 (m); δ(C–N) = 1294 (m); δ(Si–CH_3) = 1250 (s); δ (BC_3): 1182 (s); δ (C–H): 1152 (s); δ (Si–CH_2–Si) = 1049 cm^{-1} (s); δ (CH_3) = 850 cm^{-1}(s); ν (Si–C) = 780 (s).

2.3. Two-step precursor heat-treatment

As synthesized polymers were placed in alumina boats to be introduced in a sealed tube under argon atmosphere to prevent any oxygen contamination of the samples during the transfer to the furnace. Powders were then introduced under argon flow into a silica tube from a horizontal furnace (Carbolite BGHA12/450B). The tube was then evacuated (0.1 mbar) for 30 min and refilled with argon (99.995%) to atmospheric pressure. Subsequently, the samples were subjected to a cycle of ramping of 5 °C.min^{-1} to 1000 °C in flowing argon (dwelling time of 2 h at 1000 °C). A constant flow (120 mL min^{-1}) of argon was passed through the tube during the pyrolysis cycle. After cooling under argon atmosphere, samples were stored in a glove-box for characterization. Samples were labeled P-T with P the type of polymer, i.e., A, **ATi**, AB and **ABTi** and T being the two first digits of the temperature at which the polymer had been exposed. For the high temperature (T > 1000 °C) investigation, samples pyrolyzed at 1000 °C were subsequently introduced in a graphite furnace (Nabertherm VHT-GR) for heat-treatments. The furnace was pumped under vacuum (1.10^{-1} mbar), refilled with argon and maintained under a constant flow of argon (200 mL min^{-1}) during the whole heat treatment. The program consisted of a 5 °C.min^{-1} heating ramp up to the maximum temperature fixed in the range 1400–1800 °C, dwelling at the selected temperature for 2 h and cooling down to RT at 5 °C.min^{-1}. Samples were labeled P-T with P the type of polymer, i.e., A, **ATi**, AB and **ABTi** and T the two first digits of the temperature at which the polymer had been exposed (1400, 1600 and 1800 °C).

2.4. Pellet preparation

In order to design nanocomposite objects, the **ABTi** sample was introduced in a sealed stainless-steel bowl in the glove-box to be then ball milled at 200 rpm for 40 min before being warm-pressed. Then, 1 g of each ball-milled sample was introduced in a heated steel die (AINT-25-H with a 25 mm internal diameter) in the glove-box then uniaxially pressed using a Specac Atlas Autotouch Press-40T at 74 MPa or 100 MPa and heated to the set temperature (from 100 to 110 °C) at a heating rate of 5 °C/min. The selected temperature and pressure were held for 0.5 h. The pressure on the samples was then slowly deloaded during cooling down to RT within 1 h. Typical dimensions of the cylindrical green bodies were of a diameter of 25 mm and a thickness of 1.5 mm. The procedure to perform the pyrolysis and heat-treatment were similar to those applied for powders. As a change, the samples were subjected to a cycle of ramping of 1 °C.min^{-1} to 1000 °C, dwelling there for 2 h, and then cooling down to RT at 2 °C.min^{-1}. For the high temperature (T > 1000 °C) investigation, the samples underwent a heating program through a cycle of ramping of 5 °C.min^{-1} to various temperatures in the range 1000–1800 °C, dwelling at the selected temperature for 2 h and then cooling down to RT at 5 °C.min^{-1}.

2.5. Characterization

The chemical structure of the polymers was determined by transmission FTIR spectroscopy using a Nicolet Magna 550 Fourier transform-infrared spectrometer. The liquid-state ^{1}H NMR data of AHPCS were obtained from a Bruker AVANCE 300 spectrometer using $CDCl_3$ as a deuterated solvent. The ^{13}C and ^{29}Si solid-state NMR spectra of solid samples were recorded with a Bruker AVANCE 300 spectrometer using 4- or 7-mm Bruker probes at a spinning frequency of 5 or 10 kHz. ^{13}C CP MAS experiments were performed with ramped-amplitude cross-polarization in the ^{1}H channel to transfer magnetization from ^{1}H to ^{13}C. (Recycle delay = 3 s, CP contact time = 1 ms, optimized ^{1}H spinal-64 decoupling). Single pulse ^{29}Si MAS NMR spectra were recorded with a recycle delay of 60 s. Chemical shift values were referenced to tetramethylsilane for ^{13}C and ^{29}Si. The ^{11}B solid state NMR spectra were recorded on a Bruker AVANCE 700 spectrometer using a 4 mm Bruker probe and a spinning frequency of 12 kHz. They were acquired using a spin-echo θ-τ-2θ pulse sequence with $\theta = 90°$, to overcome problems related to the probe signal. The τ delay (83 μs) was synchronized with the spinning frequency. The chemical shift values were referenced to BF_3OEt_2 for ^{11}B. The static $^{47,47}Ti$ NMR experiments were recorded on a Bruker AVANCE 700 spectrometer using a 4 mm Bruker probe. A DFS−WURST−QCPMG sequence [38–40] was used. Chemical shifts were referenced to $TiCl_4$ for ^{49}Ti. Chemical analyses of the polymers were performed using a combination of several methods at Mikroanalytisches Labor Pascher (Remagen, Germany). Thermogravimetric analyses (TGA) of samples were performed in flowing argon at 5 °C.min^{-1} to 1000 °C using alumina crucibles at ambient atmospheric pressure (STA 449 F3, Netzsch GmbH, Selb, Germany) coupled with a mass spectrometer (Omnistar, Pfeiffer Vacuum GmbH, Asslar, Germany) at the outlet. The phase composition of ceramic samples - ground as fine powders – were analyzed from XRD data obtained with a Bruker D8 Advance diffractometer. The scan was performed using the CuKα1/2 radiations, from 20 to 90° 2θ with a step size of 0.02° and acquisition time of 0.9 s per step. The diffraction patterns were analyzed using the Diffrac + EVA software with the JCPDS-ICDD database. Raman

spectroscopy microanalyses were carried out with a Renishaw InViaReflex using 2 excitation laser wavelengths of 532 nm and 785 nm. High-temperature TG analyses of samples pyrolyzed at 1000 °C were done up to 1800 °C using a Setaram, Setsys apparatus at a heating rate of 5 °C/min in flowing argon. Samples were observed by JEOL IT300 scanning electron microscope. These microstructural observations were completed by chemical analyses using an Oxford X-ray dispersive spectrometer (EDX). Elemental analyses of the pyrolyzed powders were completed by instrumental gas analysis (IGA) techniques for carbon (C) content measurements using a Horiba Emia-321V and for oxygen (O), nitrogen (N) and hydrogen (H) content measurements using a Horiba EMGA-830. The silicon (Si) and titanium (Ti) contents were determined by Inductively Coupled Plasma-Optical Emission Spectrometry (ICP-OES) using a PerkinElmer Optima 8300 instrument. To investigate it, the materials are first mineralized (dissolved using a strong acid medium). All the compositions have been normalized to $Si_{1.0}$. Further observation on powders was done by transmission electron microscopy (TEM) with a JEOL JEM 2100F. The density of nanocomposite objects was investigated by hydrostatic weighing and compared to those of crushed powders studied by Helium pycnometry (Micromeritics, AccucPyc II 1340). Two spectrophotometers were used to measure the total spectral reflectance of the bulk samples. Over the wavelength range from 0.28 to 2.5 μm, the near-normal hemispherical reflection spectrum was acquired using a PerkinElmer Lambda 100 spectrophotometer. Over the wavelength range from 2.5 μm to 25 μm, the hemispherical directional reflectance (R∩,θ) was recorded using a Shimadzu UV 3600UV–vis–NIR spectrophotometer. A mathematical treatment (Mathematica software) was used to get access to the final optical parameters such as the emittance ε (infrared region) and the absorbance α (UV–visible region) from the spectroscopy data.

3. Results and discussion

3.1. Precursor syntheses

Our first attempt consisted to perform the reaction between AHPCS selected as a SiC matrix precursor and a low molecular weight compound (tetrakis(dimethylamino)titanium, TDMATi) acting as a TiC_xN_{1-x} precursor leading to the **ATi** sample. The latter was first characterized by FTIR spectroscopy to confirm the **ATi** sample structure. Data were compared to those of AHPCS, labeled A, to highlight the main changes occurring in the structure of AHPCS after chemical modification.

The FTIR spectrum of A (Fig. 2a) shows a series of bands attributed to the bonds and groups commonly identified in AHPCS [41,42]. The main changes observed in the spectrum of the **ATi** sample (Fig. 2a) are the decrease of the relative intensity of the band assigned to Si–H bonds (2115 cm^{-1}) with respect to the intensity of the Si–CH_3 band (1251 cm^{-1}) while the set of bands in the range of 2800–2950 cm^{-1} broadened

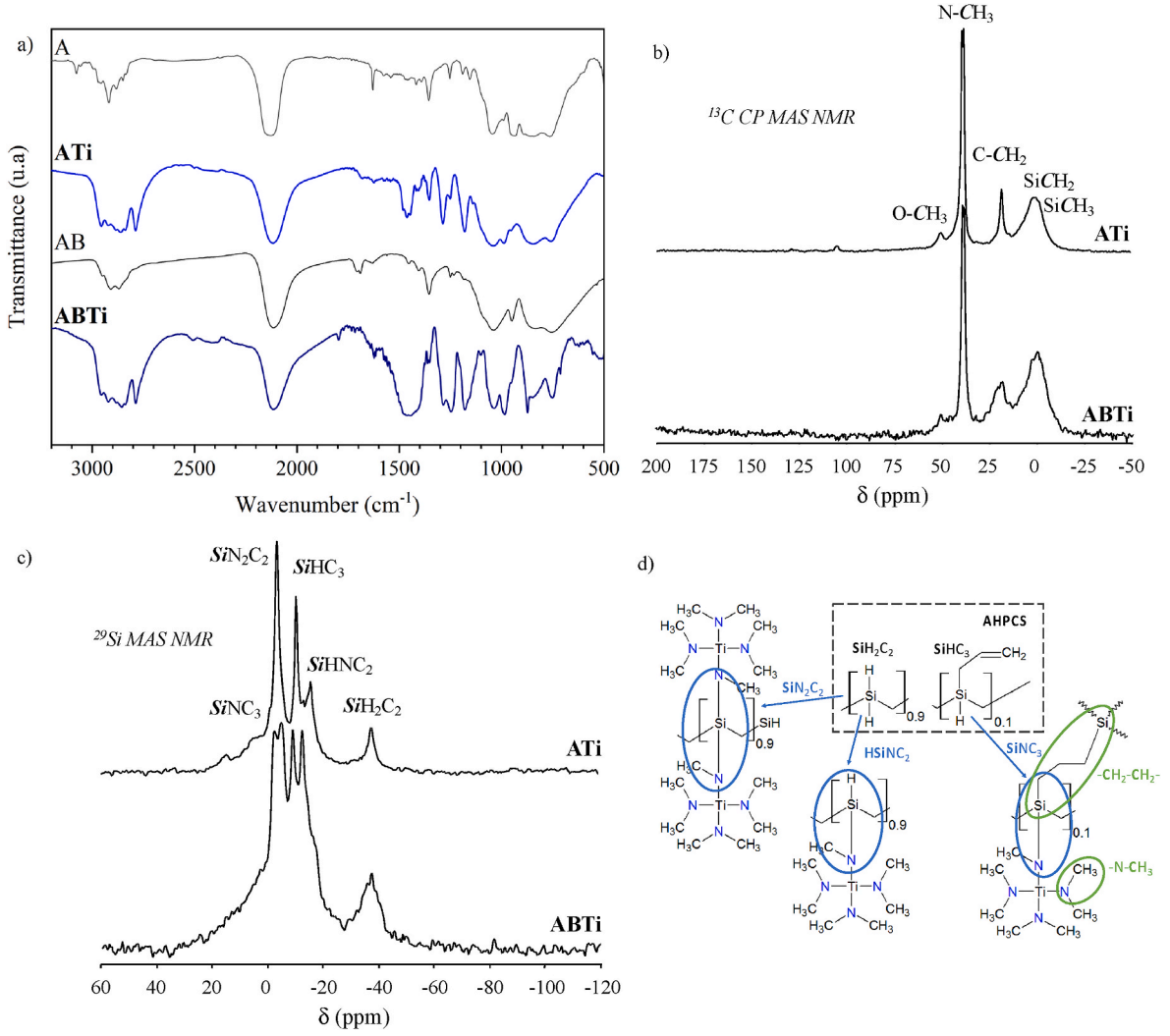

Fig. 2. a) FTIR spectra of **A**, **AB**, **ATi5** and **ABTi5**, b) ^{13}C CP MAS NMR and c) ^{29}Si MAS NMR spectra recorded for **ATi** and **ABTi** and d) main structural motifs present in Ti-modified AHPCS based on combined FTIR and NMR spectroscopies.

and two new bands appeared at 2791 cm^{-1} (C–H stretching in NCH_3 units) and 1457 cm^{-1} (NCH_3 bending). The latter highlights the introduction of $–NCH_3$ groups from TDMATi in the structure of AHPCS. To corroborate this assumption, the bands appearing in the spectrum of the **ATi** sample around 1290 cm^{-1} can be tentatively attributed to N–C bond stretching. Based on these observations and according to previous reports [23,25,26,28,33], FTIR spectroscopy confirms the establishment of Si–N(CH_3)–Ti linkages in the **ATi** sample via the reaction of SiH groups present in A with TDMATi releasing methane. Beside this, it should be pointed out a decrease of the intensity of bands assigned to the vibration of C–H bond in the allyl groups present in AHPCS (1611 cm^{-1} (C═C stretch in $CH═CH_2$) and 3076 cm^{-1} (C–H stretch in $CH_2–CH═CH_2$)). This suggests that polymerization of the allyl groups and/or hydrosilylation reaction of the latter (with Si–H units) - leading to the formation of carbosilane chains (-Si-C-C-C-Si-) - occurred. As the hydrosilylation process starts at temperatures of *ca.* 100–120 °C [40] and that reaction of AHPCS and TDMATi occurs at toluene reflux (around 120 °C), this reaction can be envisioned; especially considering the catalytic activity of TDMA*TM* (*TM* = Ti, Zr, Hf) toward hydrosilylation [22,27,32].

To achieve a better understanding of the local carbon and silicon environments in the polymer, ^{13}C and ^{29}Si solid-state NMR spectra of the polymers were recorded (Fig. 2b–c). The cross-polarization (CP) technique was used for ^{13}C NMR experiments to obtain spectra with reasonable acquisition times and signal-to-noise ratios. The ^{13}C CP MAS NMR spectrum of **ATi** (Fig. 2b) exhibits four signals around 0, 20, 39 and 50 ppm. The signal around 0 ppm is very broad and can be safely assigned to carbon atoms of aliphatic groups bonded to a silicon atom [43,44]. The large width of the signal can be due to the presence of two contributions involving $SiCH_x$ (x = 2 and 3) unit-containing environments: Si***C***H_2 groups from the polycarbosilane backbone and pendant Si***C***H_3 groups. The resonance around 20 ppm attributed to C–CH_2 units is consistent with the fact that hydrosilylation reactions and/or polymerization of allyl groups occurred in the system [37]. This is confirmed with the absence of signals at 115 and 135 ppm in the spectrum of the **ATi** sample. The signal around 39 ppm appears as a doublet and might be assigned to carbon atoms linked to nitrogen, thereby N–***C***H_3 units in two types of environments, *i.e.,* SiC_2RN (R = H or CH_2) and/or SiC_2N_2, as already proposed for a polymer resulting from the reaction between AHPCS and TDMAHf (Hf = Hafnium) [23]. The signal around 50 ppm is tentatively attributed to an $–OCH_3$ environment already present in AHPCS [37]. To complete our investigation, the experimental solid-state ^{29}Si MAS NMR spectrum of the **ATi** sample was recorded at 7T (Fig. 2c). It is composed of a set of 5 signals: those around −11 and – 38 ppm are already identified in the ^{29}Si NMR spectrum of AHPCS and reported in the literature [45,46]. They can be assigned to ***Si***HC_3 and ***Si***H_2C_2 units, respectively. Additional signals not observed in AHPCS are attributed to H***Si***NC_2 environments at −18 ppm and to ***Si***N_2C_2 at −5 ppm whereas there is also a shoulder around 5 ppm that is assigned to ***Si***NC_3 environments [35,47–49]. Thus, solid-state NMR spectroscopy confirms the introduction of Ti in the AHPCS network via the formation of Si–N(CH_3)–Ti- bridges. The main structural motifs composing the **ATi** sample are summarized in Fig. 2d.

However, although we succeeded in the synthesis of a preceramic polymer containing Si, C, N, Ti and H elements as a potential nanocomposite precursor, the shaping potential of **ATi**, a highly viscous gel, remained poor. Thus, we could not form any shape that could be useful to investigate the spectral selectivity of the derived nanocomposite objects after the thermochemical conversion and crystallization. Because we targeted the preparation of pellets, the warm-pressing (WP) process can be envisioned [34]. However, a solid sample has to be prepared. As a consequence, we introduced boron in the **ATi** sample network via the quantitative hydroboration of AHPCS with BDMS (atomic Si:B ratio of 30) leading to the intermediate AB sample [36,37] prior its reaction with TDMATi. The chemical modification of AHPCS by BDMS leads to a solid compound - AB - which can be warm-pressed at 120 °C under a pressure of 74 MPa to produce boron-doped SiC pellets by a heat-treatment at high temperatures (1000–1500 °C) [36,37]. Thus, we suggested that the post-modification of AB with TDMATi leading to the **ABTi** sample should not impair the WP ability of AB; in contrast, it would be even more appropriate toward WP because the reaction with TDMATi introduces $N(CH_3)_x$ (x = 1 and 2) units as shown via FTIR and NMR spectroscopies that are well known to act as plasticizers during a shaping at low temperature (< 200 °C) [50,51]. The **ABTi** sample – a solid compound as expected - was thoroughly characterized by FTIR and solid-state NMR spectroscopies as presented in Fig. 2 along with the results obtained from the **ATi** sample. Data have been compared to those of the AB sample [37].

The FTIR spectra of **ABTi** and **ATi** samples (Fig. 2a) are similar. The main changes are the broadness of the bands at around 1450 cm^{-1} and 1150 cm^{-1}. Especially, the band at around 1150 cm^{-1} seems to contain two contributions and especially one in the higher wavenumber domain around 1180 cm^{-1}. It could represent the signature of a trigonal planar coordination of boron connected to three carbon atoms, expected at 1181 cm^{-1} [52–54]. The investigation of the ^{13}C and ^{29}Si solid-state NMR spectra (Fig. 2b and c) confirms the similar structures between the **ATi** and **ABTi** samples; thereby the pre-addition of boron into AHPCS does not alter the further reaction with TDMATi. Indeed, nitrogen is incorporated at molecular scale in the **ABTi** sample because of the presence of signals attributed to N***C***H_3 environments in the ^{13}C NMR spectrum of the sample **ABTi** (Fig. 2b) and ***Si***NC_3 (~5 ppm), ***Si***N_2C_2 (~-5 ppm) and ***Si***HNC_2 (~-18 ppm) in the ^{29}Si NMR spectrum (Fig. 2c). However, the relative intensity of the signals is modified and the ^{29}Si NMR signal related to Si–N bonds is very broad. This tends to indicate a higher degree of crosslinking of the **ABTi** sample compared to **ATi**. This confirms that the pre-addition of B to A forming AB represents the determining factor to increase the crosslinking degree of **ABTi**.

^{11}B NMR investigations show the presence of a much broader signal in the spectrum of the **ABTi** sample compared to that identified in the spectrum of the AB sample (which was characterized again in the present paper, see Fig. 1SI in ESI). In the latter, as the boron content is very low, and because it was difficult to explain the formation of ***B***H_3C and ***B***H_4 environments, we assumed that the main signal is attributed – in part – to boron-oxidized environments, *i.e.*, BO_4 groups (δ_{iso} ~ 0 ppm) and probably also BO_3 [37]. The signal identified in the spectrum of the **ABTi** sample tends to be extended toward higher shifts indicating heterogeneity in the local chemical environment of boron atoms. We suggested that the nitrogen present in the systems can have also an impact: during their investigations of a boron-modified poly-(-allylmethylsilazane) by ^{11}B NMR spectroscopy, Berger et al. observed signals between 5 and 30 ppm assigned to trigonally coordinated boron BN_3 units, and indicated that the presence of B–C bonds is unlike [54]. In addition, BN_2H, BNH_2 and BCNH environments were identified at 28–31 ppm, 37–38 ppm and 39–43 ppm, respectively [54]. Thus, the presence of B–O (abstraction of oxygen atoms from AHPCS and/or atmosphere) and B–N bonds (abstraction of nitrogen atoms from $N(CH_3)_2$ groups) in the **ABTi** sample can be envisioned although their content is expected to be low according to the low boron content in the polymer as indicated in Table 1.

Empirical formulas reported in Table 1 confirm the incorporation of nitrogen, titanium and/or boron in the AHPCS network after reaction with BDMS and/or TDMATi. Compared to the chemical formula of AHPCS ($[Si_{1.0}C_{1.5}H_{4.2}]_n$, the elemental analysis data of **ATi** and **ABTi** samples - which respectively allowed to determine a chemical formula of $[Si_{1.0}Ti_{0.2}C_{3.2}N_{1.0}H_{8.8}]_n$ and $[Si_{1.0}B_{0.03}Ti_{0.2}C_{2.8}N_{0.7}H_{7.8}]_n$ - confirm that:

i) B does not hinder the further addition of Ti at atomic scale as confirmed by the calculated Si:Ti ratio of 5 in both samples,
ii) C, N and H contents significantly increase in the **ATi** and **ABTi** samples.

Based on the empirical formulas, the increase of the C, N and H

Table 1
Elemental composition of the polymers (*Normalyzed to total 100 wt % (total of wt% was above 98.5 wt%) and reference to $Si_{1.0}$. Oxygen content (below 2 wt%) omitted in the empirical formulae*).

Samples	Element content (wt%)							Empirical formulas
	Si	B	Ti	C	N	H	O	
A	54.8	–	–	35.0	–	8.3	1.9	$Si_{1.0}C_{1.5}H_{4.2}$
AB	52.9	0.7	–	35.6	–	8.9	1.9	$Si_{1.0}B_{0.03}C_{1.6}H_{4.7}$
ATi	27.5	–	10.7	37.8	13.7	8.7	1.6	$Si_{1.0}Ti_{0.2}C_{3.2}N_{1.0}H_{8.8}$
ABTi	31.8	0.4	9.1	38.1	10.2	8.9	1.5	$Si_{1.0}B_{0.03}Ti_{0.2}C_{2.8}N_{0.7}H_{7.8}$

contents is most probably related to a high portion of -Ti[N(CH$_3$)$_2$]$_x$ (x = 1 to 3) units as side groups that do not further react during the synthesis progress. Thus, we can conclude that the **ATi** and **ABTi** samples display a higher degree of crosslinking than AHPCS because of the formation of carbosilane chains, -Si–N(CH$_3$)–Ti- bridges (in both **ATi** and **ABTi**) and/or B–O, B–C and/or B–N bond-based units (in **ABTi**). Their networks is surrounded by pendant –N(CH$_3$)$_2$ groups. Before investigating the design of pellets by WP of **ABTi**, we investigated its conversion into nanocomposites as powders.

3.2. Polymer to ceramic conversion

In this section, we discuss the thermal behavior of the **ABTi** sample up to 1000 °C in flowing argon as monitored by TG experiments (Fig. 3a). Its behaviour has been compared to those of AHPCS (A), AB and **ATi** recorded in the same conditions.

The TG behavior of AHPCS (A) is well referenced in the literature [23,37,41,42] with three distinct and consecutive weight losses leading to a final ceramic yield (mass of the polymer/mass of the resulting ceramics) around 72%.

In our previous report, we highlighted the positive impact of the incorporation of boron in AHPCS (atomic Si:B ratio of 30) to significantly increase its ceramic yield (Fig. 3a) [37]. Herein, the AB sample confirmed the increase of the ceramic yield by 19% compared to A as referenced in Ref. [37].

The reaction of TDMATi with A and AB leads to the **ATi** and **ABTi** samples which display a similar TG profile with a one-step weight loss occurring mainly in the temperature range 200–600 °C. Compared to A, the 125–250 °C temperature range behavior of **ATi** shows a lower weight loss because the distillation of low molecular weight species at

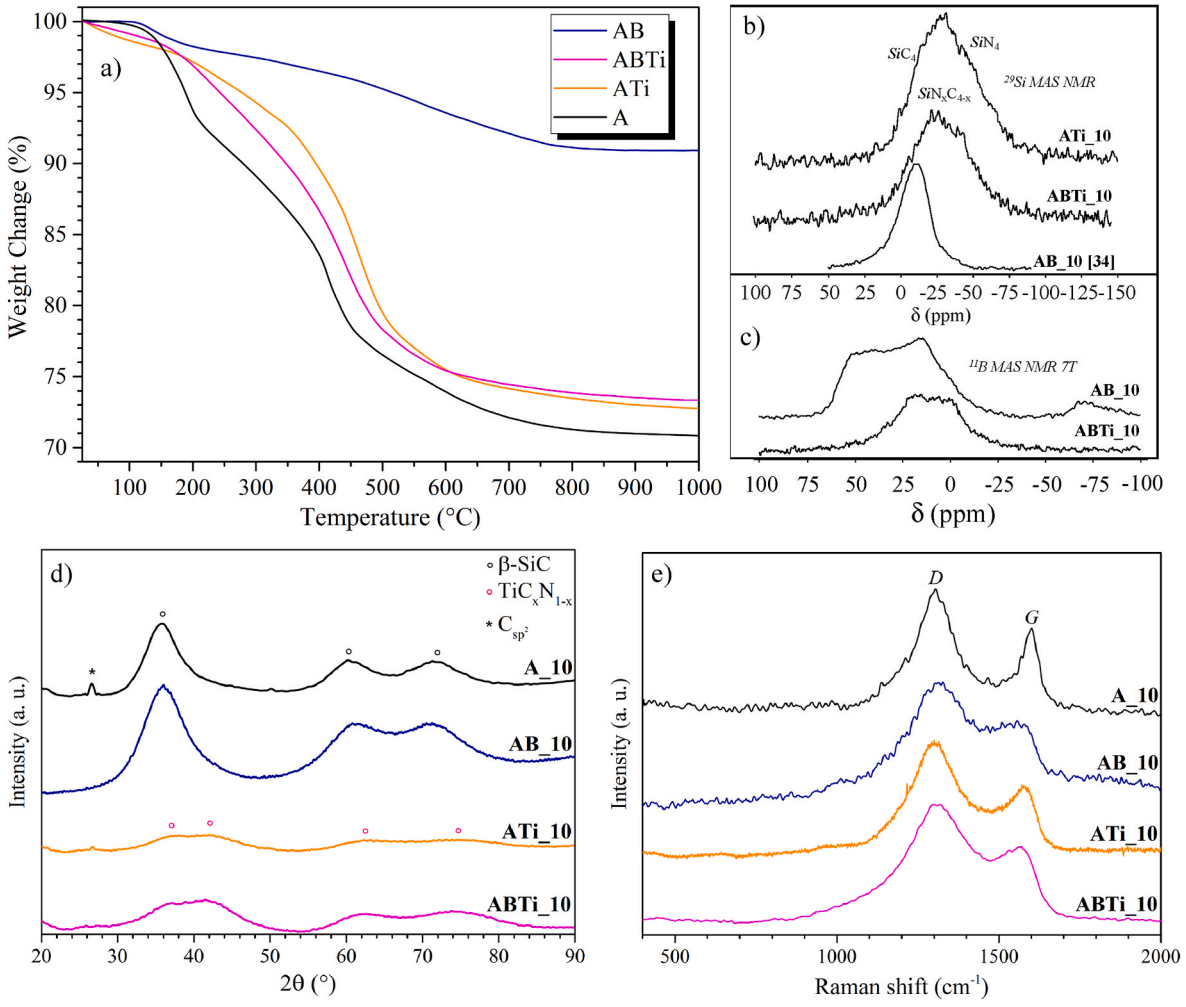

Fig. 3. a) TG curves recorded during the decomposition of A, AB, **ATi** and **ABTi** samples in flowing argon, b) ^{29}Si MAS NMR and c) ^{11}B MAS NMR spectra recorded for AB_10, **ATi_10** and **ABTi-10** and d) XRD patterns and e) Raman spectra of A_10, AB_10, **ATi_10** and **ABTi_10** samples.

low temperature is reduced. This confirms that the degree of cross-linking of **ATi** is higher than that of A. In contrast, the decomposition of **ATi** is accelerated at intermediate temperature (450–600 °C) compared to A: it is associated with a release of dimethylamine ($m/z = 44$; See Fig. 2SI in ESI) fragments (not identified for AHPCS) indicating the occurrence of condensation reactions involving side groups of the type $–N((CH_3)_2)_x$ ($x = 1 \rightarrow 3$). This is even more obvious by observing the TG behavior of the **ABTi** sample which exhibits a much higher weight loss than AB while being similar to **ATi**. This observation indicated that **ATi** and **ABTi** contain a high portion of $–N(CH_3)_2$ groups as side groups in their structure mainly responsible of their weight loss occurring at intermediate temperature through the release of dimethylamine (See Fig. 2SI in ESI).

After pyrolysis at 1000 °C, ^{29}Si MAS NMR spectra (Fig. 5a) of the samples labeled **ATi_10** (obtained from the **ATi** sample) and **ABTi_10** (obtained from the **ABTi** sample) display a signal centered around −25 ppm attributed to multi units going from **Si**C_4 unit positions such as those identified in the spectra of A_10 (not shown) and AB_10 [37] (coming from the native polymer, AHPCS (sample A)) as reported in Fig. 3b to **Si**N_4 unit positions (i.e., formation of $Si–N(CH_3)–Ti$- bridges in the **ATi** and **ABTi** samples) [28]. As a consequence, we attributed this broad signal to **Si**C_xN_{4-x} ($0 \leq x \leq 4$) units [48,49,53]. It should be pointed out that ^{13}C CP MAS NMR spectra could not be recorded owing to the lack of protons after a pyrolysis up to 1000 °C.

The ^{11}B MAS NMR spectrum of the **ABTi_10** sample (Fig. 3c) shows a broad resonance ranging from −25 to +40 ppm, which could correspond to several environments including amorphous B_4C [55], BC_xO_{3-x} ($x = 0$, 1, 2) [37] and BN_3 groups [50]. In comparison, the ^{11}B MAS spectrum of the AB_10 sample (formed by the pyrolysis of AB at 1000 °C) showed a larger signal that extends up to 70 ppm suggesting the presence of B_4C, BC_xO_{3-x} ($x = 0$, 1, 2) and BC_3 [37]. Thus, solid-state ^{11}B MAS NMR confirms that the post-addition of TDMATi on AB affects the boron environment in the derived ceramics by developing B–N bonds in the material.

The diffuse peaks in the XRD patterns of the **ATi_10** and **ABTi_10** samples (Fig. 3d) reveal that as-pyrolyzed samples are poorly crystallized with a very small crystal size. They display the signature of a face-centered cubic (fcc) TiN phase (powder diffraction file (ICDD PDF number: 00-038-1420)) according to the positions at 2θ around 36.5°, 42.6°, 62.3 and around 75.0° attributable to the (111), (200), (220) and (311) reflections, respectively. However, because we cannot exclude the presence of TiC (ICDD PDF: 00-032-1383) regarding the identification of diffuse peaks; we assigned those peaks to the TiC_xN_{1-x} ($0 \leq x \leq 1$) phase resulting from the solid solution between TiC and TiN. The XRD patterns of the **ATi_10** and **ABTi_10** samples are clearly different from those recorded for the A_10 and AB_10 samples which exhibit broad peak characteristic of a β-SiC phase (ICDD PDF number: 00-029-1129; (111), (220) and (311) peaks) and sp^2 C ((002) peak). Thus, this tends to indicate that the presence of the TiC_xN_{1-x} ($0 \leq x \leq 1$) phase in the **ATi_10** and **ABTi_10** samples inhibits the crystallization of SiC. The presence of sp^2 C was confirmed in all the materials by Raman spectroscopy (Fig. 3e) through the appearance of the bands of the defect-induced D (coming from the breathing mode A_{1g} of the sp^2 rings) and graphitic G bands (arising from the stretching mode E_{2g} of the sp^2 C–C bonds) at ~1310 cm^{-1} and ~1600 cm^{-1}, respectively. Because the D-mode is caused by disordered structure in sp^2-hybridized carbon systems and considering that the G band is characteristic of highly ordered carbon species, the I(D)/I(G) ratio - similar in all sample - confirms the relatively high degree of disorder in all samples prepared at 1000 °C.

Previous results are highly reflected in the chemical formula of the sample determined by EDX (Table 2). Although EDX is not appropriate for light elements such as B, C, N and O, there is a clear tendency: data of the **ATi_10** and **ABTi_10** samples demonstrate that the initial Si:Ti atomic ratio fixed in the polymers (Si:Ti = 5) is more or less retained in the derived ceramics (Si:Ti = 3.7–3.9) and that they confirm the presence of nitrogen. All ceramics display an excess of carbon considering that carbon can be linked to Si and Ti (and possibly to B for boron-containing samples). It should be pointed out that C, N, O and H contents of the **A_10** and **ATi_10** samples have been measured by IGA. techniques (see experimental part) for more accuracy. In addition, the Si and Ti contents were measured by ICP-OES (see experimental part). It is obvious that the carbon and nitrogen contents significantly increased in Ti-containing samples as expected. Therefore, Ti-containing samples prepared at 1000 °C are made of a highly disordered SiC_xN_{4-x} ($0 \leq x \leq 4$) phase, sp^2 C and possibly boron carbide, oxide and/or nitride phases in which a TiC_xN_{1-x} phase ($0 \leq x \leq 1$) nucleated.

3.3. High temperature behaviour of materials prepared at 1000 °C

As-pyrolyzed samples appear to be stable up to 1400 °C although the reference A_10 and AB_10 samples seem to be slightly decomposed most probably according to the evolution of hydrogen from the ceramic network in this temperature range as already discussed in our previous paper [56]. Above 1400 °C, different behaviours are observed. A fast and single weight loss continuously occurs up to 1700 °C for the **ATi_10** and **ABTi_10** samples. In contrast, the weight loss recorded for the A_10 sample is relatively low – although continuous up to 1800 °C - and the boron-containing samples systematically display a higher weight loss compared to their boron-free counterparts.

Because of the presence of oxygen in the A_10 sample (Table 2), the measured weight loss can be attributed to the evolution of gaseous species containing oxygen, such as CO and SiO [57]. The latter easily reacts with free carbon to form stoichiometric SiC at a higher temperature. Considering also the presence of a low oxygen content in other samples, these reactions might be responsible of a minor part of the decomposition of Ti-modified ceramics above 1400 °C. However, such materials also contain nitride or carbonitride phases which have been identified by solid NMR spectroscopy and XRD. Such phases are also well known to undergo carbothermal reduction reactions above 1450 °C involving nitrogen and therefore inducing a weight loss [58]. Thus, the

Table 2
Elemental composition of the samples pyrolyzed at 1000 °C estimated by EDX and for the samples **A_10** and **ATi_10** by ICP (Si and Ti) and by hot gas extraction techniques (C, N, O, H).

Samples	Element content (wt%)							Empirical formula
	EDX							
	Si	B	Ti	C	N	O		
A_10	56	–	–	40	–	4		$Si_{1.0}C_{1.7}$
AB_10	49	5	–	41	–	5		$Si_{1.0}B_{0.3}C_{2.0}$
ATi_10	37	–	16	25	13	7		$Si_{1.0}Ti_{0.3}C_{1.7}N_{0.7}$
ABTi_10	26	3	12	36	20	3		$Si_{1.0}B_{0.3}Ti_{0.3}C_{3.2}N_{1.5}$
	ICP (Si, Ti) and hot gas extraction (C, N, O, H)							
	Si	B	Ti	C	N	O	H	
A_10	58.9	–	–	36.5		3.6	1.0	$Si_{1.0}C_{1.5}H_{0.5}O_{0.1}$
ATi_10	33.9	–	15.1	33.0	14.1	3.5	0.4	$Si_{1.0}Ti_{0.3}C_{2.3}N_{0.8}H_{0.3}O_{0.2}$

large weight loss recorded for the **ATi_10** and **ABTi_10** samples is mainly attributed to the decomposition of the carbonitride phases that compose them including SiC_xN_{4-x} ($0 \leq x \leq 4$), TiC_xN_{1-x} ($0 \leq x \leq 1$) and B(C)N phases by free carbon. The higher weight losses recorded for boron-containing samples is difficult to explain but could be related to the highest nitrogen content of these materials (see Table 2). To support this discussion, we first investigated solid-state ^{29}Si and ^{47,49}Ti NMR spectroscopy (Fig. 4b and c), Raman spectroscopy and XRD (Fig. 5) of intermediates isolated at 1400 °C, 1600 °C and 1800 °C.

The investigation of the ^{29}Si MAS NMR spectrum (Fig. 4b) confirms the relative stability of **ATi_10** and **ABTi_10** upon heat treatment to 1400 °C under argon. **Si**C_xN_{4-x} ($0 \leq x \leq 4$) environments are still identified in the spectra of **ATi_14**, and **ABTi_14** samples. A radical change is observed from 1400 °C to 1800 °C, in good agreement with the behaviour observed by TGA. **ATi_18** and **ABTi_18** exhibit only **Si**C_4 environments on the ^{29}Si MAS NMR spectra confirming the occurrence of carbothermal reduction reactions above 1450 °C; thereby the decomposition of the SiC_xN_{4-x} ($0 \leq x \leq 4$) units into SiC_4 units. Carbothermal reduction reactions are also confirmed with the investigation of the ^{47,49}Ti NMR spectra of the **ATi_14**, **ATi_18** and **ABTi_18** samples (Fig. 4c). ^{47,49}Ti NMR spectra of TiC and TiN were recorded as references and are consistent with those previously reported in the literature [59] with ^{49}Ti resonances centered around −300 and −750 ppm and ^{47}Ti resonances centered around −600 and −1000 ppm in TiC and TiN, respectively. Both NMR active isotopes of titanium (Ti) have almost identical gyromagnetic ratios so that even at 16.4 T the resonance frequencies differ only by a few kHz. Moreover, they have relatively large quadrupole moments ($Q(^{47}Ti) = 0.29.10^{28}$ m^2, $Q(^{47}Ti) = 0.24.10^{28}$ m^2) resulting in large signals with overlapped resonances from the two isotopes.

Whereas at a temperature of 1400 °C (**ATi_14**) the large signal shows a maximum at about −1000 ppm suggesting that Ti elements are predominantly bound to N elements, the signal is shifted at less negative chemical shift values at 1800 °C (**ATi_18** and **ABTi_18**). This indicates that a part of N atoms is replaced by C atoms in the coordination sphere of Ti atoms, again confirming the occurrence of carbothermal reduction reactions above 1400 °C, here the reaction of the TiC_xN_{1-x} phase ($0 \leq x \leq 1$) with free carbon. In contrast to SiC_xN_{4-x} ($0 \leq x \leq 4$) units which are fully converted into SiC_4 units, the Ti-based phase still contain residual nitrogen even after a heat-treatment at 1800 °C. To support these findings, we analyzed the evolution of the free carbon phase in the **ABTi_14**, **ABTi_16** and **ABTi_18** samples by Raman spectroscopy (Fig. 5a) and XRD (Fig. 5b). Related data for **ABTi_14**, **ABTi_16** and **ABTi_18** samples are presented in Fig. 4SI in ESI.

The presence of the free carbon phase was confirmed in all the materials at all temperatures from 1400 to 1800 °C through the appearance of the bands of the defect-induced D and graphitic G bands (Fig. 5a). In addition to these bands, the **ATi_18** (see Fig. 3SIa in ESI), **ABTi_16** (Fig. 5a) and **ABTi_18** (Fig. 5a) samples showed a band identified as the traversal optical band of the cubic phase of SiC at 780 cm^{-1}, thereby confirming solid-state ^{29}Si MAS NMR data. All these previous observations are deeply highlighted by X-ray diffraction (Fig. 5b) performed on the same samples.

ATi_14 (see Fig. 3SIb in ESI) and **ABTi_14** (Fig. 5b) samples show

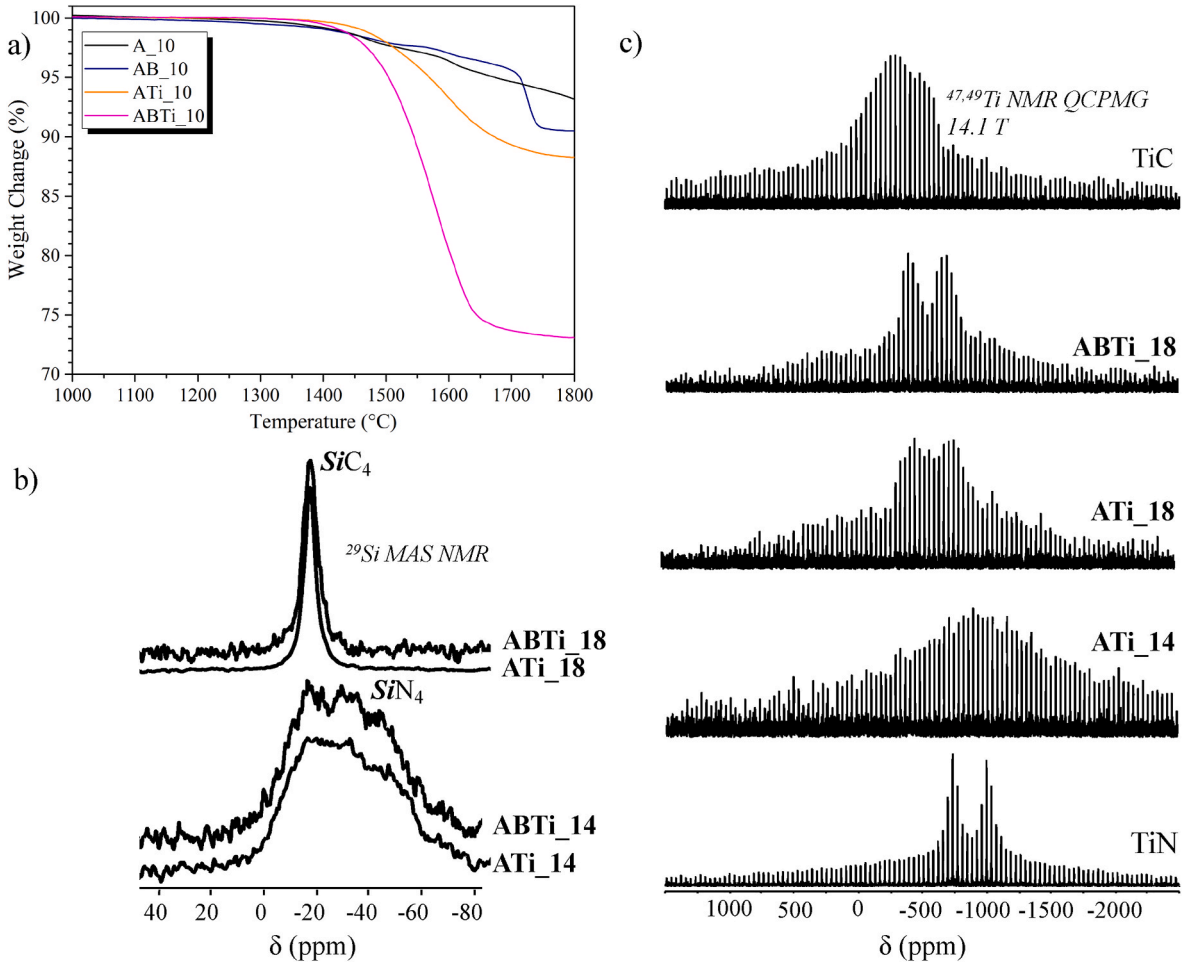

Fig. 4. a) TG curves recorded during the decomposition of A_10, AB_10, **ATi_10** and **ABTi_10** samples in flowing argon, b) ^{29}Si MAS NMR and c) ^{47,49}Ti NMR QCPMG spectra recorded for **ATi_14**, **ABTi_14** (only ^{29}Si), **ATi_18** and **ABTi-18**.

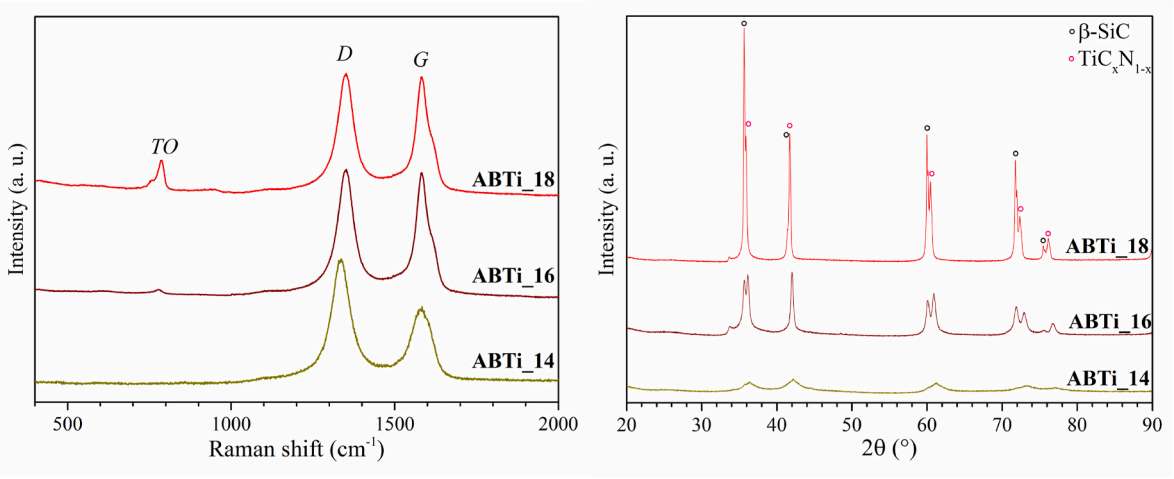

Fig. 5. a) Raman spectra and b) XRD patterns of **ABTi_X** samples with X = 14, 16 and 18.

only broad peaks in their similar XRD patterns that can belong to very large TiC_xN_{1-x} ($0 \leq x \leq 1$) crystals. These broad peaks are at a mid-position between the two references that could be approximated by the Vegard law [60] to a $TiC_{0.5}N_{0.5}$ phase. When increasing the heat-treatment temperature, a β-SiC phase (ICDD PDF: 00-029-1129) is identified in both patterns of **ATi_16** (see Fig. 3SIb in ESI) and **ABTi_16** (Fig. 5b) confirming the crystallization of the matrix. This TiC_xN_{1-x} ($0 \leq x \leq 1$)/β-SiC composite structure is confirmed at higher temperature through the XRD patterns of **ATi_18** (see Fig. 3SIb in ESI) and **ABTi_18** (Fig. 5b). According to the Vegard law of peaks position of the TiC_xN_{1-x} ($0 \leq x \leq 1$) phase, final compositions of $TiC_{0.87}N_{0.13}$ and $TiC_{0.95}N_{0.05}$ for the nanophase are calculated for **ATi_18** and **ABTi_18**, respectively. They confirm that nitrogen is still bonded to Ti even after heat-treatment to 1800 °C.

To assess the phase micro-/nanostructure of these materials, the **ATi_14** sample has been investigated by TEM (Fig. 6). Because previously investigated characterization showed close similarities between the **ATi_14** and **ABTi_14** samples, only the former has been investigated. Then, we investigated both **ATi_18** (Fig. 7a and b) and **ABTi_18** (Fig. 7c and d) samples. Fig. 6a depicts a **ATi_14** specimen consisting of homogeneously dispersed small nuclei (dark contrast) embedded in a featureless matrix characteristic of an amorphous network. The Selected Area Electron Diffraction (SAED) pattern (insets in Fig. 6a) identifies distinct rings which can be indexed to the (111), (200) and (220) planes of a TiC_xN_{1-x} phase ($0 \leq x \leq 1$) at 0.255, 0.221 and 0.157 nm, respectively. The higher magnification image in Fig. 6b isolates nanocrystals with a size ranging from 3 to 6 nm and a fringe spacing of 0.25 nm matching the (111) lattice fringe of a TiC_xN_{1-x} ($0 \leq x \leq 1$) phase. These nanocrystals are surrounded by an amorphous matrix containing sp^2 carbon ribbons. As a consequence, the materials prepared at 1400 °C (**ATi_14** and **ABTi_14**) can be described as nanocomposites made of TiC_xN_{1-x} nanocrystals surrounded by free carbon and an amorphous matrix; most probably SiC_xN_{4-x} ($0 \leq x \leq 4$) as identified by solid-state NMR.

Fig. 7 displays the TEM images of the **ATi_18** (Fig. 7a) and **ABTi_18** (Fig. 7b and c) samples. The increase of the heat-treatment temperature to 1800 °C (**ATi_18** sample) highlights the highest crystallinity of the material made of two populations of crystal size. The corresponding EDX mapping and SAED patterns made of distinct spots identify TiC_xN_{1-x} as the smallest crystals (size below 100 nm) and SiC representing the biggest crystals. A same level of crystalline quality and similar TiC_xN_{1-x} nanocrystal sizes are identified in the **ABTi_18** sample (Fig. 7b). The corresponding SAED pattern (inset of Fig. 7b) is composed of distinct

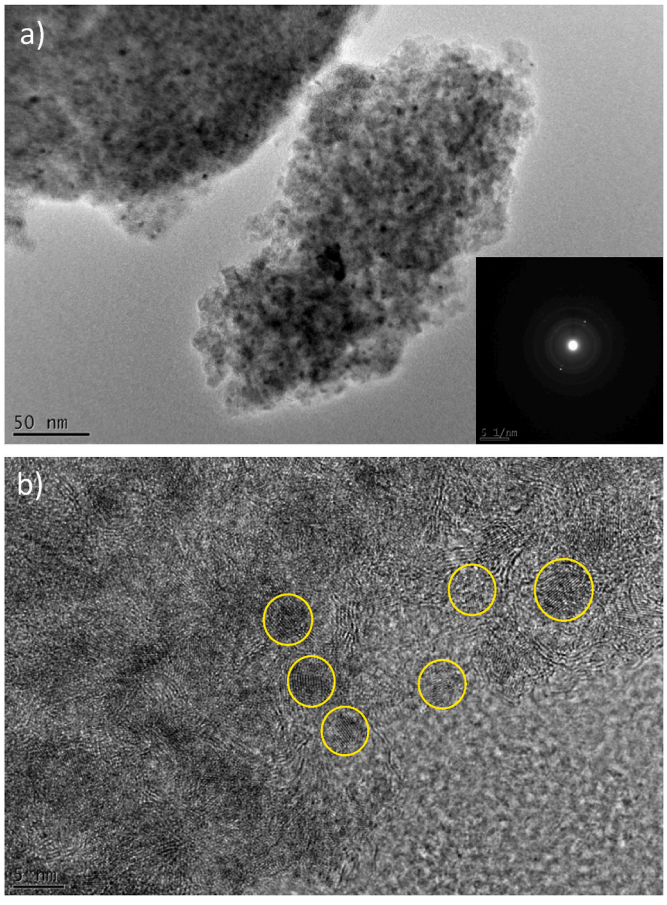

Fig. 6. (a) Low magnification TEM image of the surface with the corresponding selected area electron diffraction pattern as insert and b) HRTEM image of the **ATi_14** sample.

spots that are ascribed to the (111), (200), (220), (311) and (222) planes of the fcc structure of TiC_xN_{1-x}. The TEM micrograph of the **ABTi_18** sample in Fig. 7c shows that the crystalline TiC_xN_{1-x} nanoparticles display a generally hexagonal shape which renders the generation of a particle size distribution quite difficult.

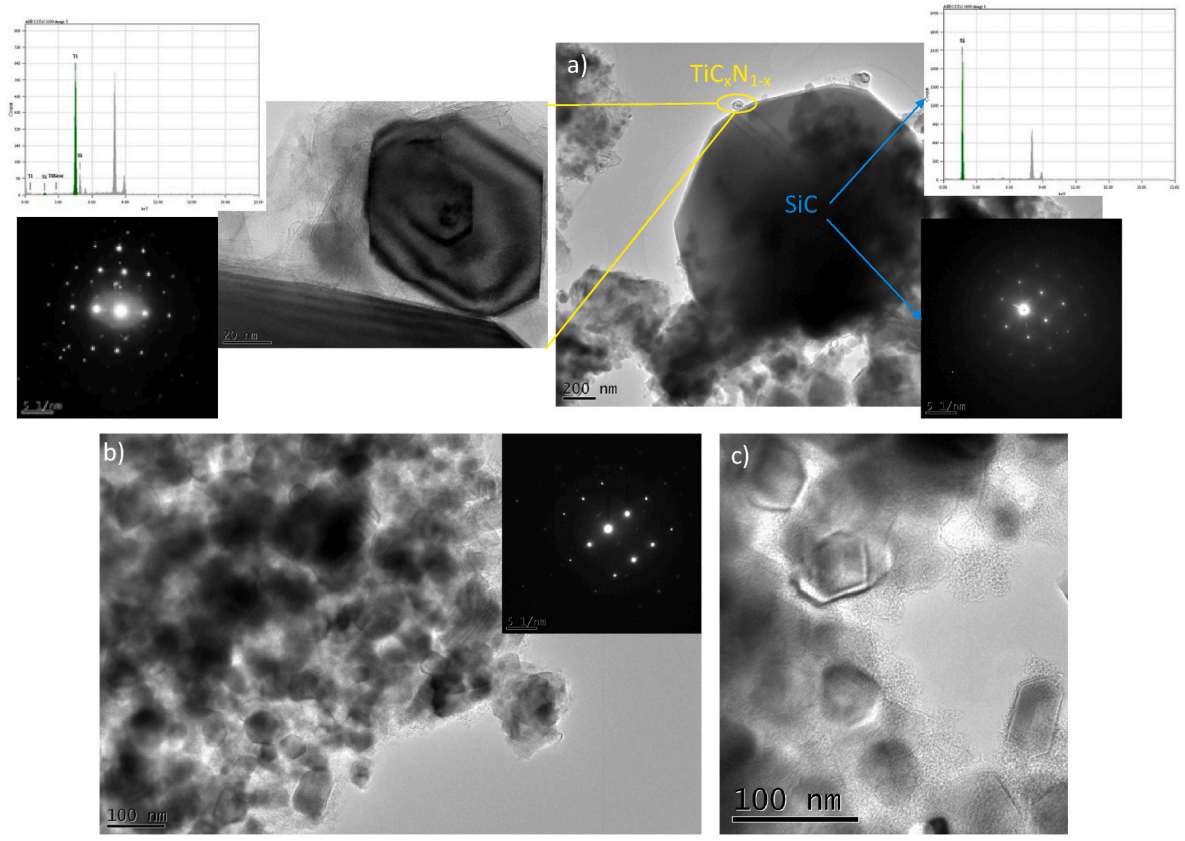

Fig. 7. (a) Low magnification TEM image of the **ATi_18** sample with the corresponding selected area electron diffraction patterns and EDX spectra identifying TiC_xN_{1-x} and SiC crystals, b) low magnification TEM image of the **ABTi_18** sample and c) HRTEM image of a TiC crystal identified in the **ABTi_18** sample.

3.4. Spectral selectivity of nanocomposite objects

As mentioned previously, the **ABTi** sample is shaped into pellets in order to investigate – as a proof of concept - the room temperature (RT) spectral selectivity of the derived nanocomposites in the solar spectrum. Thus, we have prepared the ABTi_X samples (X = 10, 14, 16 and 18) as pellets by integrating a warm-pressing (WP) stage after the synthesis of **ABTi**. The **ABTi** sample exhibits sufficient plasticity to be warm-pressed at 110 °C for 30 min under 80 MPa and form crack-free pieces after pyrolysis at 1000 °C (**ABTi_10**). Then, the samples have been heat-treated in the temperature range 1400 °C (**ABTi_14**) - 1800 °C (**ABTi_18**) in flowing argon to follow the evolution of the textural properties (Table 3) and hemispherical reflectance (Fig. 8) of pellets according to their temperature of preparation. It should be mentioned that pellets display similar XRD patterns than those recorded for powder analogs (See Fig. 4SI in ESI).

Table 3 gathers the results obtained from hydrostatic weight of bulk analogs (ρ_a apparent density, ρ_b bulk density and O.P Open Porosity).

The bulk density increases with the temperature of preparation according to the extended crystallization of the materials. However, data also show that the carbothermal reduction reactions previously discussed develop an open porosity in the bulk **ABTi_16** and **ABTi_18** samples, especially if compared to bulk samples derived from AB (i.e., AB_18). It has been reported that the total hemispherical emissivity can notably increase with the increase of the surface roughness/porosity [11]. For instance, an increase of the porosity from 5 to 30 vol% in HfC-based materials led to significant gain of emissivity from 0.4 to 0.55 [11]; thereby a decrease of the selectivity. Within this context, the effect of the temperature of preparation of these materials on their RT spectral selectivity which is defined by the absorptance:emittance ratio [61] has

Table 3
Densities determined by hydrostatic weight for bulk, (ρ_a apparent density, ρ_b bulk density and O.P Open Porosity).

Samples	ρ_a (g.cm^{-3})	ρ_b (g.cm^{-3})	O.P (%)
ABTi_10	2.15	2.29	6
ABTi_14	2.28	2.57	11
ABTi_16	1.98	3.18	38
ABTi_18	2.34	3.27	29
AB_18	2.33	2.85	18

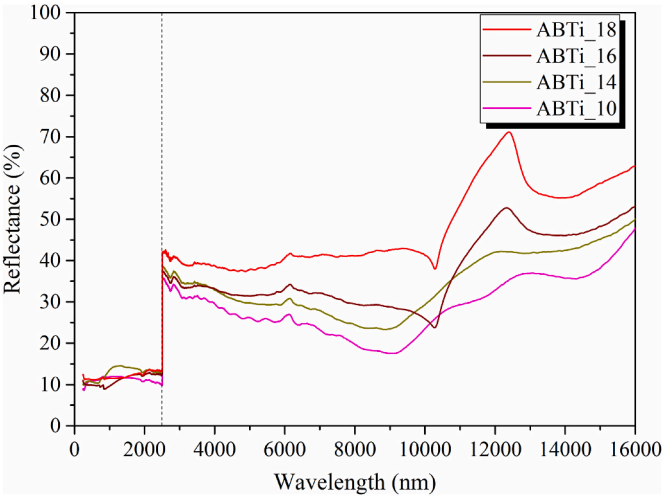

Fig. 8. Hemispherical reflectance of the ABTi_X (X = 10, 14, 16 and 18) samples.

been investigated. Absorbance in the solar spectrum wavelength and emittance in the infrared one are both related to hemispherical reflectance by Kirchhoff law. Fig. 8 plots the evolution of the hemispherical reflectance versus the wavelength for the ABTi_X samples (X = 10, 14, 16, 18).

As expected, the reflectance is very low below λ = 2500 nm and is independent of the temperature of preparation of the samples. It is close to expectation for an ideal SSA in the solar spectrum. Then, above λ = 2500 nm (where it should reach 1 for an ideal SSA), the reflectance evolution is directly linked to the temperature at which the sample is prepared. In particular, the **ABTi_18** sample demonstrated the highest and more stable reflectance in the wavenumber range 2500–10000 nm. At 10000 nm, the reflectance evolves through the Christiansen point which is due to absorption mechanisms in the far-infrared range (lattice vibration), causing the material to behave like a blackbody (low reflectance = high emissivity, assuming Kirchhoff's law of radiation) [62]. Thus, above 10000 nm, the reflectance profile is characteristic of a highly crystallized SiC phase [63] in the **ABTi_18** sample (also in the **ABTi_16** sample) as shown with the AB_18 sample (See Fig. 5SI in ESI). The highly crystallized SiC phase in the **ABTi_18** and AB_18 samples leads to a higher hemispherical reflectance above 2500 nm and therefore a better general selectivity value as calculated from Fig. 8 and reported in Table 4.

In Table 4, we can clearly observe the contribution of the TiC_xN_{1-x} phase *in situ* generated in the SiC matrix for the **ABTi_18** sample. It shows a selectivity increased by more than 20% (up to 1.675) compared to the AB_18 sample. This value represents one of the highest selectivity reported so far for SiC-based materials [63–65], especially by considering the relatively high porosity of the materials and the presence of residual carbon. Thus, further works will consist to minimize the high porosity of these materials and investigated SiC precursor leading to a lower free carbon content in the derived SiC matrix.

4. Conclusion

Within the present study, titanium and/or boron-modified polycarbosilanes (AHPCS) have been synthesized and used as precursors of SiC-based nanocomposites. The chemistry behind the polymer synthesis and pyrolysis was investigated in details and the high temperature behaviour of derived amorphous ceramics was critically followed. Whereas the addition of Ti at molecular scale introduced side groups that affected the weight change of AHPCS during the further polymer-to-ceramic conversion, the incorporation of B allowed increasing the crosslinking degree of the Ti-modified polycarbosilane to allow forming pellets by warm-pressing. The final nano-/microstructure evolved according to the heat-treatment temperature fixed in the range 1000–1800 °C. The amorphous single-phase ceramics produced at 1000 °C led to nanocrystalline-TiC_xN_{1-x} ($0 \leq x \leq 1$)/amorphous-SiC_xN_{4-x} ($0 \leq x \leq 4$) nanocomposites after heat-treatment at 1400 °C. In the temperature range of 1400–1800 °C, a large weight loss occurred in the samples involving the release of nitrogen to form porous and highly crystallized nanocomposites composed of TiC_xN_{1-x} ($0 \leq x \leq 1$) and SiC crystals with free carbon. The highest spectral selectivity is reached with the samples prepared at 1800 °C which is the results of the presence of the TiC_xN_{1-x} ($0 \leq x \leq 1$) crystals confined in the SiC matrix. However, there is still room for further studies on optimizing the spectral selectivity of these materials by considering specific process parameters that can contribute to increase the TiC(N) volume fraction while decreasing the porosity and free carbon. In addition, high temperature selectivity is required to confirm the benefit of these nanaocomposite structures compared to monolithic SiC. These opportunities are now being addressed. It is anticipated that this will lead to SiC-based nanocomposites with a high optical selectivity.

Table 4
RT selectivity calculated for the bulk samples, and an ideal solar behavior (i.e., as high as possible for absorptivity and selective ratio, and as low as possible for emissivity).

Samples	α, absorptance	ε, emittance	α/ε, selectivity
ABTi_10	0.887	0.734	1.208
ABTi_14	0.883	0.678	1.302
ABTi_16	0.900	0.644	1.398
ABTi_18	0.886	0.529	1.675
AB_10	0.899	0.754	1.192
AB_18	0.887	0.652	1.360
Ideal solar absorbers	1	0	∞

Declaration of competing interest

The authors declare that they have no known competing financial interests or personal relationships that could have appeared to influence the work reported in this paper.

Acknowledgements

Dr. Samuel Bernard, Dr. Maxime Balestrat, Dr. Xavier Deschanels, Dr. Audrey Soum-Glaude, Dr. Fabrice Rossignol and Dr. Nicolas Pradeilles acknowledge Agence Nationale de la Recherche (ANR) for supporting this work through the Carapass project (PhD thesis of Maxime Balestrat, Project N° ANR-16-CE08-0026-01). Dr. Samuel Bernard thanks the Nouvelle-Aquitaine region and CTTC for the financial support of the PhD thesis of Maxime Cheype. The French Région Ile de France - SESAME program - is acknowledged for financial support (700 MHz spectrometer).

Appendix A. Supplementary data

Supplementary data to this article can be found online at https://doi.org/10.1016/j.oceram.2023.100353.

References

[1] P. Heller, The Performance of Concentrated Solar Power (CSP) Systems: Analysis, Measurement and Assessment, Woodhead Publishing, 2017, https://doi.org/10.1016/C2014-0-03695-7.
[2] N. Calvet, A.H. Slocum, A. Gil, B. Grange, R. Lahlou, T.T. Hamer, M. Diago, M. Tetreault-Friend, D.S. Codd, D.L. Trumper, P.R. Armstrong, Dispatchable solar power using molten salt directly irradiated from above, Sol. Energy 220 (2021) 217–229, https://doi.org/10.1016/j.solener.2021.02.058.
[3] C.E. Kennedy, Review of Mid- to High-Temperature Solar Selective Absorber Materials, National Renewable Energy Lab., Golden, CO. (US), 2002, https://doi.org/10.2172/15000706.
[4] L. Noč, I. Jerman, Review of the spectrally selective (CSP) absorber coatings, suitable for use in SHIP, Sol. Energy Mater. Sol. Cell. 238 (2022), 111625, https://doi.org/10.1016/j.solmat.2022.111625.
[5] J.J. Cuomo, J.F. Ziegler, J.M. Woodall, A new concept for solar energy thermal conversion, Appl. Phys. Lett. 26 (1975) 557–559, https://doi.org/10.1063/1.87990.
[6] I. Cañadas, V.M. Candelario, G. De Aloysio, J. Fernández, L. Laghi, S. Cuesta-López, Y. Chen, T.J. Marrow, A. Rinaldi, A.M. Sanchez, A. Tatì, C. Testani, Characterization of solar-aged porous silicon carbide for concentrated solar power receivers, Materials 14 (2021) 4627, https://doi.org/10.3390/ma14164627.
[7] V. Casalegno, L. Ferrari, M. Jimenez Fuentes, A. De Zanet, S. Gianella, M. Ferraris, V.M. Candelario, High-performance SiC–based solar receivers for CSP: component manufacturing and joining, Materials 14 (2021) 4687, https://doi.org/10.3390/ma14164687.
[8] M.J.H. Balat, Determination of the active-to-passive transition in the oxidation of silicon carbide in standard and microwave-excited air, J. Eur. Ceram. Soc. 16 (1996) 55–62, https://doi.org/10.1016/0955-2219(95)00104-2.
[9] E. Sani, L. Mercatelli, F. Francini, J.-L. Sans, D. Sciti, Ultra-refractory ceramics for high-temperature solar absorbers, Scripta Mater. 65 (2011) 775–778, https://doi.org/10.1016/j.scriptamat.2011.07.033.
[10] E. Sani, L. Mercatelli, P. Sansoni, L. Silvestroni, D. Sciti, Spectrally selective ultra-high temperature ceramic absorbers for high-temperature solar plants, J. Renew. Sustain. Energy 4 (2012), 033104, https://doi.org/10.1063/1.4717515.
[11] E. Sani, L. Mercatelli, J.-L. Sans, L. Silvestroni, D. Sciti, Porous and dense hafnium and zirconium ultra-high temperature ceramics for solar receivers, Opt. Mater. 36 (2013) 163–168, https://doi.org/10.1016/j.optmat.2013.08.020.

[12] E. Sani, L. Mercatelli, M. Meucci, A. Balbo, L. Silvestroni, D. Sciti, Compositional dependence of optical properties of zirconium, hafnium and tantalum carbides for solar absorber applications, Sol. Energy 131 (2016) 199–207, https://doi.org/10.1016/j.solener.2016.02.045.
[13] K. Xu, M. Du, L. Hao, J. Mi, Q. Yu, S. Li, A review of high-temperature selective absorbing coatings for solar thermal applications, Journal of Materiomics 6 (2020) 167–182, https://doi.org/10.1016/j.jmat.2019.12.012.
[14] H. Aréna, M. Coulibaly, A. Soum-Glaude, A. Jonchère, A. Mesbah, G. Arrachart, N. Pradeilles, M. Vandenhende, A. Maitre, X. Deschanels, SiC-TiC nanocomposite for bulk solar absorbers applications: effect of density and surface roughness on the optical properties, Sol. Energy Mater. Sol. Cell. 191 (2019) 199–208, https://doi.org/10.1016/j.solmat.2018.11.018.
[15] H. Aréna, M. Coulibaly, A. Soum-Glaude, A. Jonchère, G. Arrachart, A. Mesbah, N. Pradeilles, M. Vandenhende, A. Maître, X. Deschanels, Effect of TiC incorporation on the optical properties and oxidation resistance of SiC ceramics, Sol. Energy Mater. Sol. Cell. 213 (2020), 110536, https://doi.org/10.1016/j.solmat.2020.110536.
[16] B. Du, X. Wang, Z. Zou, Microstructure and tribological behavior of laser in situ synthesized TiC-reinforced Fe-based composite coatings, Tribol. Lett. 43 (2011) 295–301, https://doi.org/10.1007/s11249-011-9808-4.
[17] P.J. Martin, R.P. Netterfield, W.G. Sainty, C.G. Pacey, The preparation and characterization of optical thin films produced by ion-assisted deposition, J. Vac. Sci. Technol. A 2 (1984) 341–345, https://doi.org/10.1116/1.572735.
[18] S. Shimada, T. Ishil, Oxidation kinetics of zirconium carbide at relatively low temperatures, J. Am. Ceram. Soc. 73 (1990) 2804–2808, https://doi.org/10.1111/j.1151-2916.1990.tb06678.x.
[19] S. Shimada, A thermoanalytical study on the oxidation of ZrC and HfC powders with formation of carbon, Solid State Ionics 149 (2002) 319–326, https://doi.org/10.1016/S0167-2738(02)00180-7.
[20] A. Onuma, H. Kiyono, S. Shimada, M. Desmaison, High temperature oxidation of sintered TiC in an H2O-containing atmosphere, Solid State Ionics 172 (2004) 417–419, https://doi.org/10.1016/j.ssi.2004.02.067.
[21] C. Zou, L. Huang, J. Wang, S. Xue, Effects of antireflection layers on the optical and thermal stability properties of a spectrally selective CrAlN–CrAlON based tandem absorber, Sol. Energy Mater. Sol. Cell. 137 (2015) 243–252, https://doi.org/10.1016/j.solmat.2015.02.010.
[22] R. Perrem, F. Henry, G. Peraudeau, B. Armas, R. Berjoan, E. Beche, An XPS and thermogravimetric study of oxidized AlN and AlN–Si3N4 layers deposited by liquid-phase chemical vapour deposition, J. Mater. Sci. 5 (1997) 1305–1312, https://doi.org/10.1023/A:1018556606993.
[23] Q. Wen, Y. Xu, B. Xu, C. Fasel, O. Guillon, G. Buntkowsky, Z. Yu, R. Riedel, E. Ionescu, Single-source-precursor synthesis of dense SiC/HfCxN1−x-based ultrahigh-temperature ceramic nanocomposites, Nanoscale 6 (2014) 13678–13689, https://doi.org/10.1039/C4NR03376K.
[24] Q. Wen, Z. Yu, R. Riedel, E. Ionescu, Single-source-precursor synthesis and high-temperature evolution of a boron-containing SiC/HfC ceramic nano/micro composite, J. Eur. Ceram. Soc. 41 (2021) 3002–3012, https://doi.org/10.1016/j.jeurceramsoc.2020.05.031.
[25] M.C. Bechelany, V. Proust, C. Gervais, R. Ghisleni, S. Bernard, P. Miele, In situ controlled growth of titanium nitride in amorphous silicon nitride: a general route toward bulk nitride nanocomposites with very high hardness, Adv. Mater. 26 (2014) 6548–6553, https://doi.org/10.1002/adma.201402356.
[26] M.C. Bechelany, V. Proust, A. Lale, P. Miele, S. Malo, C. Gervais, S. Bernard, Nanocomposites through the chemistry of single-source precursors: understanding the role of chemistry behind the design of monolith-type nanostructured titanium nitride/silicon nitride, Chem. Eur J. 23 (2017) 832–845, https://doi.org/10.1002/chem.201603661.
[27] A. Lale, V. Proust, M.C. Bechelany, A. Viard, S. Malo, S. Bernard, A comprehensive study on the influence of the polyorganosilazane chemistry and material shape on the high temperature behavior of titanium nitride/silicon nitride nanocomposites, J. Eur. Ceram. Soc. 37 (2017) 5167–5175, https://doi.org/10.1016/j.jeurceramsoc.2017.04.001.
[28] M. Balestrat, A. Lale, A.V.A. Bezerra, V. Proust, E.W. Awin, R.A.F. Machado, P. Carles, R. Kumar, C. Gervais, S. Bernard, In-situ synthesis and characterization of nanocomposites in the Si-Ti-N and Si-Ti-C systems, Molecules 25 (2020) 5236, https://doi.org/10.3390/molecules25225236.
[29] A. Lale, M.D. Mallmann, S. Tada, A. Bruma, S. Özkar, R. Kumar, M. Haneda, R. A. Francisco Machado, Y. Iwamoto, U.B. Demirci, S. Bernard, Highly active, robust and reusable micro-/mesoporous TiN/Si3N4 nanocomposite-based catalysts for clean energy: understanding the key role of TiN nanoclusters and amorphous Si3N4 matrix in the performance of the catalyst system, Appl. Catal. B Environ. 272 (2020), 118975, https://doi.org/10.1016/j.apcatb.2020.118975.
[30] E. Ionescu, S. Bernard, R. Lucas, P. Kroll, S. Ushakov, A. Navrotsky, R. Riedel, Polymer-derived ultra-high temperature ceramics (UHTCs) and related materials, Adv. Eng. Mater. 21 (2019), 1900269, https://doi.org/10.1002/adem.201900269.
[31] G. Mera, M. Gallei, S. Bernard, E. Ionescu, Ceramic nanocomposites from tailor-made preceramic polymers, Nanomaterials 5 (2015) 468–540, https://doi.org/10.3390/nano5020468.
[32] G. Mera, E. Ionescu, Silicon-containing preceramic polymers, in: Encyclopedia of Polymer Science and Technology, John Wiley & Sons, Ltd, 2013, https://doi.org/10.1002/0471440264.pst591.
[33] J. Yuan, S. Hapis, H. Breitzke, Y. Xu, C. Fasel, H.-J. Kleebe, G. Buntkowsky, R. Riedel, E. Ionescu, Single-source-precursor synthesis of hafnium-containing ultrahigh-temperature ceramic nanocomposites (UHTC-NCs), Inorg. Chem. 53 (2014) 10443–10455, https://doi.org/10.1021/ic501512p.
[34] O. Majoulet, F. Sandra, M.C. Bechelany, G. Bonnefont, G. Fantozzi, L. Joly-Pottuz, A. Malchère, S. Bernard, P. Miele, Silicon–boron–carbon–nitrogen monoliths with high, interconnected and hierarchical porosity, J. Mater. Chem. A. 1 (2013) 10991–11000, https://doi.org/10.1039/C3TA12119D.
[35] A. Viard, D. Fonblanc, M. Schmidt, A. Lale, C. Salameh, A. Soleilhavoup, M. Wynn, P. Champagne, S. Cerneaux, F. Babonneau, G. Chollon, F. Rossignol, C. Gervais, S. Bernard, Molecular chemistry and engineering of boron-modified polyorganosilazanes as new processable and functional SiBCN precursors, Chem. Eur J. 23 (2017) 9076–9090, https://doi.org/10.1002/chem.201700623.
[36] C. Durif, M. Wynn, M. Balestrat, G. Franchin, Y.-W. Kim, A. Leriche, P. Miele, P. Colombo, S. Bernard, Open-celled silicon carbide foams with high porosity from boron-modified polycarbosilanes, J. Eur. Ceram. Soc. (2019), https://doi.org/10.1016/j.jeurceramsoc.2019.08.012.
[37] M. Schmidt, C. Durif, E.D. Acosta, C. Salameh, H. Plaisantin, P. Miele, R. Backov, R. Machado, C. Gervais, J.G. Alauzun, G. Chollon, S. Bernard, Molecular-level processing of Si-(B)-C materials with tailored nano/microstructures, Chem. Eur J. 23 (2017) 17103–17117, https://doi.org/10.1002/chem.201703674.
[38] L.A. O'Dell, R.W. Schurko, QCPMG using adiabatic pulses for faster acquisition of ultra-wideline NMR spectra, Chem. Phys. Lett. 464 (2008) 97–102, https://doi.org/10.1016/j.cplett.2008.08.095.
[39] I. Hung, Z. Gan, On the practical aspects of recording wideline QCPMG NMR spectra, J. Magn. Reson. 204 (2010) 256–265, https://doi.org/10.1016/j.jmr.2010.03.001.
[40] O. Pauvert, F. Fayon, A. Rakhmatullin, S. Krämer, M. Horvatić, D. Avignant, C. Berthier, M. Deschamps, D. Massiot, C. Bessada, 91Zr nuclear magnetic resonance spectroscopy of solid zirconium halides at high magnetic field, Inorg. Chem. 48 (2009) 8709–8717, https://doi.org/10.1021/ic9007119.
[41] V. Proust, M.C. Bechelany, R. Ghisleni, M.-F. Beaufort, P. Miele, S. Bernard, Polymer-derived Si-C-Ti systems: from titanium nanoparticle-filled polycarbosilanes to dense monolithic multi-phase components with high hardness, J. Eur. Ceram. Soc. 36 (2016) 3671–3679, https://doi.org/10.1016/j.jeurceramsoc.2016.04.023.
[42] F. Sandra, A. Ballestero, V.L. Nguyen, M.N. Tsampas, P. Vernoux, C. Balan, Y. Iwamoto, U.B. Demirci, P. Miele, S. Bernard, Silicon carbide-based membranes with high soot particle filtration efficiency, durability and catalytic activity for CO/HC oxidation and soot combustion, J. Membr. Sci. 501 (2016) 79–92, https://doi.org/10.1016/j.memsci.2015.12.015.
[43] N.S. Choong Kwet Yive, R.J.P. Corriu, D. Leclercq, P.H. Mutin, A. Vioux, Silicon carbonitride from polymeric precursors: thermal cross-linking and pyrolysis of oligosilazane model compounds, Chem. Mater. 4 (1992) 141–146, https://doi.org/10.1021/cm00019a029.
[44] R. Li, C. Zhou, L. Yang, S. Li, J. Zhan, Z. Yu, H. Xia, Synthesis and polymer-to-ceramic conversion of tailorable copolysilazanes, J. Appl. Polym. Sci. 122 (2011) 1286–1292, https://doi.org/10.1002/app.34274.
[45] M. Huang, Y. Fang, R. Li, T. Huang, Z. Yu, H. Xia, Synthesis and properties of liquid polycarbosilanes with hyperbranched structures, J. Appl. Polym. Sci. 113 (2009) 1611–1618, https://doi.org/10.1002/app.30071.
[46] I.L. Rushkin, Q. Shen, S.E. Lehman, L.V. Interrante, Modification of a hyperbranched hydridopolycarbosilane as a route to new polycarbosilanes, Macromolecules 30 (1997) 3141–3146, https://doi.org/10.1021/ma961664p.
[47] J. Schuhmacher, F. Berger, M. Weinmann, J. Bill, F. Aldinger, K. Müller, Solid-state NMR and FT IR studies of the preparation of Si–B–C–N ceramics from-boron-modified polysilazanes, Appl. Organomet. Chem. 15 (2001) 809–819, https://doi.org/10.1002/aoc.235.
[48] A. Viard, L. Gottardo, D. Lopez-Ferber, A. Soleilhavoup, C. Salameh, S. Samal, Y. Gueguen, T. Rouxel, G. Motz, F. Babonneau, C. Gervais, S. Bernard, Molecular design of meltspinnable co-polymers as Si–B–C–N fiber precursors, Dalton Trans. 46 (2017) 13510–13523, https://doi.org/10.1039/C7DT02559A.
[49] D. Fonblanc, D. Lopez-Ferber, M. Wynn, A. Lale, A. Soleilhavoup, A. Leriche, Y. Iwamoto, F. Rossignol, C. Gervais, S. Bernard, Crosslinking chemistry of poly (vinylmethyl-co-methyl)silazanes toward low-temperature formable preceramic polymers as precursors of functional aluminium-modified Si–C–N ceramics, Dalton Trans. 47 (2018) 14580–14593, https://doi.org/10.1039/C8DT03076F.
[50] S. Duperrier, C. Gervais, S. Bernard, D. Cornu, F. Babonneau, C. Balan, P. Miele, Design of a series of preceramic B-Tri(methylamino)borazine-Based polymers as fiber precursors: architecture, thermal behavior, and melt-spinnability, Macromolecules 40 (2007) 1018–1027, https://doi.org/10.1021/ma0623035.
[51] S. Duperrier, S. Bernard, A. Calin, C. Sigala, R. Chiriac, P. Miele, C. Balan, Design of a series of preceramic B-Tri(methylamino)borazine-Based polymers as fiber precursors: shear rheology investigations, Macromolecules 40 (2007) 1028–1034, https://doi.org/10.1021/ma062304x.
[52] A. Viard, D. Fonblanc, D. Lopez-Ferber, M. Schmidt, A. Lale, C. Durif, M. Balestrat, F. Rossignol, M. Weinmann, R. Riedel, S. Bernard, Polymer Derived Si-B-C-N Ceramics: 30 Years of Research, Advanced Engineering Materials, 2018, https://doi.org/10.1002/adem.201800360.
[53] L. Gottardo, S. Bernard, C. Gervais, K. Inzenhofer, G. Motz, M. Weinmann, C. Balan, P. Miele, Chemistry, structure and processability of boron-modified polysilazanes as tailored precursors of ceramic fibers, J. Mater. Chem. 22 (2012) 7739–7750, https://doi.org/10.1039/C2JM15919H.
[54] F. Berger, A. Müller, F. Aldinger, K. Müller, Solid-state NMR investigations on Si-B-C-N ceramics derived from boron-modified poly(allylmethylsilazane), Z. Anorg. Allg. Chem. 631 (2005) 355–363, https://doi.org/10.1002/zaac.200400259.
[55] H. Werheit, T. Au, R. Schmechel, S.O. Shalamberidze, G.I. Kalandadze, A. M. Eristavi, IR-active phonons and structure elements of isotope-enriched boron carbide, J. Solid State Chem. 154 (2000) 79–86, https://doi.org/10.1006/jssc.2000.8815.

[56] M. Balestrat, E. Diz Acosta, O. Hanzel, N. Tessier-Doyen, R. Machado, P. Šajgalík, Z. Lenčéš, S. Bernard, Additive-free low temperature sintering of amorphous SiBC powders derived from boron-modified polycarbosilanes: toward the design of SiC with tunable mechanical, electrical and thermal properties, J. Eur. Ceram. Soc. 40 (2020) 2604–2612, https://doi.org/10.1016/j.jeurceramsoc.2019.12.037.

[57] S.M. Johnson, R.D. Brittain, R.H. Lamoreaux, D.J. Rowcliffe, Degradation mechanisms of silicon carbide fibers, J. Am. Ceram. Soc. 71 (1988), https://doi.org/10.1111/j.1151-2916.1988.tb05033.x. C-132-C–135.

[58] R.M. Prasad, G. Mera, K. Morita, M. Müller, H.J. Kleebe, A. Gurlo, C. Fasel, R. Riedel, Thermal decomposition of carbon-rich polymer-derived silicon carbonitrides leading to ceramics with high specific surface area and tunable micro- and mesoporosity, J. Eur. Ceram. Soc. 32 (2012) 477–484, https://doi.org/10.1016/j.jeurceramsoc.2011.08.020.

[59] K.J.D. MacKenzie, R.H. Meinhold, D.G. McGavin, J.A. Ripmeester, I. Moudrakovski, Titanium carbide, nitride and carbonitrides: a ^{13}C, ^{14}N, ^{15}N and $^{47,49}Ti$ solid-state nuclear magnetic resonance study, Solid State Nucl. Magn. Reson. 4 (1995) 193–201, https://doi.org/10.1016/0926-2040(94)00051-D.

[60] P. Duwez, F. Odell, Phase relationships in the binary systems of nitrides and carbides of zirconium, columbium, titanium, and vanadium, J. Electrochem. Soc. 97 (1950) 299, https://doi.org/10.1149/1.2777885.

[61] J.D. Macia, D.M. Herrera-Zamora, F.I. Lizama-Tzec, J. Bante-Guerra, O.E. Arés-Muzio, G./ Oskam, H. Romero-Parades Rubio, J.J. Alvarado-Gil, C. arancibia-Bulnes, V. Ramos-Sanchez, H.I. Villafan-Vidales, Optical and thermal properties of selective absorber coatings under CSP conditions, AIP Conf. Proc. 1850 (2017), https://doi.org/10.1063/1.4984492, 120001-1-120001-8.

[62] B. Rousseau, J.F. Brun, D.D.S. Meneses, P. Echegut, Temperature measurement: christiansen wavelength and blackbody reference, Int. J. Thermophys. 26 (2005) 1277–1286, https://doi.org/10.1007/s10765-005-6726-4.

[63] M. Coulibaly, G. Arrachart, A. Mesbah, X. Deschanels, From colloidal precursors to metal carbides nanocomposites MC (M=Ti, Zr, Hf and Si): synthesis, characterization and optical spectral selectivity studies, Sol. Energy Mater. Sol. Cell. 143 (2015) 473–479, https://doi.org/10.1016/j.solmat.2015.07.039.

[64] E. Sani, L. Mercatelli, D. Jafrancesco, J.L. Sans, D. Sciti, Ultra-High Temperature Ceramics for solar receivers: spectral and high-temperature emittance characterization, J. Europ. Optical Soci.- Rapid Pub. 7 (2012), https://doi.org/10.2971/jeos.2012.12052.

[65] X. Xu, Z. Rao, J. Wu, Y. Li, Y. Zhang, X. Lao, In-situ synthesis and thermal shock resistance of cordierite/silicon carbide composites used for solar absorber coating, Sol. Energy Mater. Sol. Cell. 130 (2014) 257–263, https://doi.org/10.1016/j.solmat.2014.07.017.